2017

Stochastic Analysis of a Mammalian Circadian Clock Model: Small Protein Number Effects

David W. Morgens
Stanford University, dmorgens@stanford.edu

Blerta Shtylla
Pomona College, shtyllab@pomona.edu

Stochastic Analysis of a Mammalian Circadian Clock Model: Small Protein Number Effects

Stochastic analysis of a mammalian circadian clock model: Small protein number effects

David W. Morgens[†1], Blerta Shtylla[1,*]

*Correspondence:
Blerta Shtylla, Dept. of Mathematics, Pomona College, 614 N College Ave., Claremont, CA 91711, USA
shtyllab@pomona.edu

Abstract

The circadian clock, responsible for coordinating organism function with daily and seasonal changes in the day-night cycle, is controlled by a complex protein network that constitutes a robust biochemical oscillator. Deterministic ordinary differential equation models have been used extensively to model the behavior of these central clocks. However, due to the small number of proteins involved in the circadian oscillations, mathematical models that track stochastic variations in the numbers of clock proteins may reveal more complex and biologically relevant behaviors. In this paper, we compare the response of a robust yet detailed deterministic model for the mammalian circadian clock with its corresponding stochastic version that takes into account low protein number noise. We then use signal analysis techniques in order to examine differences in behavior among components of the stochastic system oscillator. This approach reveals differences in the system response between the stochastic and deterministic model and also allows us to extend bifurcation analysis into the stochastic domain. From our analysis of the unfitted stochastic model, we propose novel explanations of some previous experimental results.

Keywords: circadian clock, stochastic model, autocorrelation, wavelet analysis

1 Introduction

A wide range of organisms employ a 24-hour circadian clock that adapts multiple system responses at the genetic, physiological and behavioral level to daily changes in the environment. At the basis of circadian rhythms is a regular, oscillating chemical reaction that is employed at the single cell level. In mammals, autonomous cell clocks are embedded in a hierarchical system in which a master pacemaker in the suprachiasmatic nucleus (SCN) entrains a network of peripheral circadian oscillators throughout the body [1]. Disrupted circadian rhythms can have serious medical implications in humans. Circadian rhythm disorders are related not only to disruption of sleep patterns, but are also associated with cognitive impairment, mood disturbances, and increased risk of cardiometabolic disorders [2]. Furthermore, circadian rhythms are beginning to gain critical importance in clinical settings as drug delivery effectiveness is affected by the rhythms of single cell metabolism that tie in the circadian networks [3].

In the last 20 years, various features of these chemical clocks have been uncovered in a variety of organisms [4, 5]. A set of common features have emerged from the simpler cyanobacteria clocks to more complex mammalian networks. It is emerging that the core circadian clock network contains two types of components: 1) activators such as KaiA in Synechococcus, Clc and Cyc in Drosophila, and Clock and Bmal in mice and humans, and 2) repressors such as KaiB/KaiC in Sychococcus, Frq in Neurospora, and Tim and Per in Drosophila and mammals. For example, in mammalian cells the Period protein (PER) creates a negative feedback loop since high levels of PER protein suppress the transcription of the Per mRNA, lowering the levels of PER protein, which then allows continued transcription of Per mRNA [6]. The inclusion of additional activators and delay within these negative feedback loops complete the picture producing a robust circadian oscillator. While in principle negative feedback and delay are sufficient to generate oscillations, what is not clear is the specific contribution of the various uncovered elements of circadian clock networks, as it is also not clear what role post-transcriptional modification plays in these oscillatory patterns. Despite the complexities of these systems, there is broad consensus that transcriptional regulation lies at the core of the circadian oscillators [1].

The accuracy of the mammalian circadian clock can be inferred by observing the behavior of rats in a dark environment. Indeed, when separated from stimuli rats are observed to continue to operate on a 24-hour cycle, defined by when they wake up or exercise. Using this

---

[1]Department of Mathematics, Pomona College, Claremont CA 91711 USA, [†] Current address: Department of Genetics, Stanford University, 300 Pasteur Drive, Stanford, CA 94305, USA

method, previous studies have found a strikingly small 2% fluctuation in the circadian period from day to day [7]. This accuracy may be due to the synchronization of the almost 20,000 individual neuron oscillators by the SCN pacemaker [8, 9]. Yet, when measurements are made at the level of a single neuronal cell, the PER proteins oscillate irregularly, with periods varying up to 3 hours from day to day [7], indicating that at the single cell level noise and heterogeneity are well tolerated [10].

Since the biochemical networks involved in producing circadian oscillatory patterns are rather complex even at the single cell scale, mathematical modeling can provide a robust framework that not only accounts for the available experimental data but also allows us to perform in silico experiments in scenarios where data collection is difficult [11]. Over the past several years, mathematical models have indeed played a central role in our understanding of these complex, circadian mechanisms. The original, and still quite influential, circadian model was proposed in 1995 to explain circadian rhythms in flies [6]. Since then, systems of ordinary differential equations (ODEs), ranging from a core 3 equations to a detailed 180 have been used to explore the behavior and effects of stimuli, mutants, and drug perturbations [12, 13].

While this approach has been powerful, ODEs describe continuous changes in concentrations assuming large protein numbers. Yet, at the single cell level internal noise can be significant due to the low protein copy numbers and the necessarily discrete nature of reactions that further translates into potentially significant perturbations in oscillation period and amplitude. While simple systems can be devised to be robust to internal noise [10], it is not so clear that the more detailed models derived from recent biological experiments retain the predicted ODE robustness in the small protein number limits. Indeed, since current evidence supports that only small numbers of molecules are involved in circadian rhythms, many circadian models have been examined as discrete stochastic systems [14, 10, 15, 12, 16].

In this paper, we take a similar approach and consider a stochastic model of a fairly detailed mammalian circadian clock proposed in Relogio et al. [17] and seek to compare the robustness of the proposed system in the limit of small protein numbers. Of particular interest to us is to employ computational techniques in order to test and uncover the key underlying oscillatory architecture in the stochastic regime where protein numbers are low. This analysis would be of interest since the data obtained from gene expression levels is necessarily noisy, and ODE fitting to averaged signals can overlook potentially important system features. Specifically, the current analysis of circadian rhythms is often limited to on/off or period/amplitude measurements. These types of measurements are well served by deterministic systems which

are similarly limited in the types of responses that they can produce and seek to match at best averaged data sets. But stochastic systems, and their biological counterparts, can display more complicated behavior with potential biological consequences. Here we study how "biochemical noise" can alter the behavior of these systems by starting from a deterministic set of ODEs describing two coupled negative feedback loops of which one is described as a robust oscillator and the second as a weaker one generated by six interacting proteins and parameterized by [17] using a wide range of published data. We created a stochastic model of the same system using the techniques described in [18] and then analyzed it using methods of signal processing analysis described in [19] and [20].

2 Mathematical Model

We start by first delineating the ODE model of Relogio et al. [17], and then we discuss our stochastic model.

2.1 The Relogio et al. ODE model

The ODE model proposed and parametrized in [17] consists of five genes and their associated proteins that can exist in complexes, nuclear and cytosolic localizations, and different phosphorylation states for a total of 19 species. Together, these form two coupled negative feedback loops, with ROR, RevErb, and BMAL making up one loop and PER and CRY the other, as highlighted in Fig. 1.
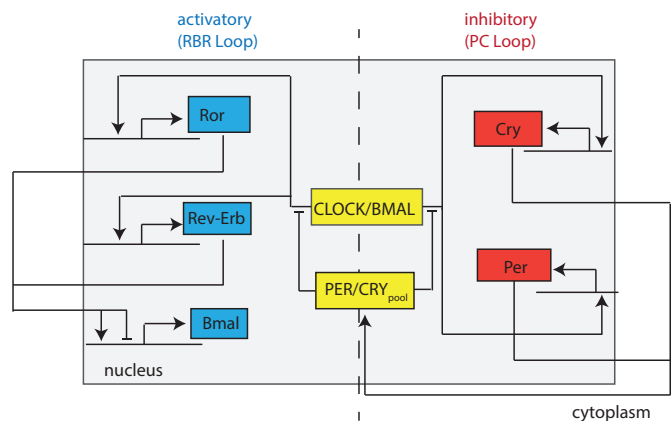
Figure 1: A diagram of the key genes and nucleus proteins involved in the two circadian loops. The model of [17] contains 19 species, here we highlight the 5 genes, shown in blue and red boxes to mark activatory vs. inhibitory action. The proteins associated with the five genes can exist as both cytoplasmic and nucleus species. For the full set of reactions involving transcription, translation, import/export and phosphorylation/dephosphorylation, see [17].

For completeness, here we highlight the key features included in the ODE model equations of [17].

PC Loop   The PC loop contains the two key inhibitory genes Cry and Per, which are translated in the cytoplasm as PER_c/CRY_c. After phosphorylation in the cytoplasm, these proteins form complexes that are imported in the nucleus. In Fig. 1, we show a PER/CRY pool of nuclear complexes comprising both phosphorylated and unphosphorylated proteins that act as inhibitors on CLOCK/BMAL activity; the PER/CRY_{pool} thus closes the negative feedback loop. The gene transcription reactions were modeled using Michaelis-Menten kinetics and Hill functions

Per $\dfrac{dy_1}{dt}$

$$= v_{1max} \frac{1 + a\left(\frac{x_1}{k_{t1}}\right)^5}{1 + \left(\frac{PC}{k_{i1}}\right)^7 \left(\frac{x_1}{k_{t1}}\right)^5 + \left(\frac{x_1}{k_{t1}}\right)^5} - d_{y1}y_1 \quad (1)$$

Cry $\dfrac{dy_2}{dt}$

$$= v_{2max} \frac{1 + d\left(\frac{x_1}{k_{t2}}\right)^7}{1 + \left(\frac{PC}{k_{i2}}\right)^4 \left(\frac{x_1}{k_{t2}}\right)^7 + \left(\frac{x_1}{k_{t2}}\right)^7} \frac{1}{1 + \frac{x_5}{k_{i21}}}$$
$$- d_{y2}y_2 \quad (2)$$

where we highlight that the Hill coefficients were fitted to gene expression data and likely indicate multiple regulatory regions involved in mRNA production, whereas d_i is the degradation rate of the Per or Cry mRNA. As shown in [21], the high nonlinearities can be reduced to obtain terms with Hill coefficients of 2 or 3 at the cost of introducing explicit delay terms in the mRNA production terms which adds to model complexity. Alternatively nonlinearities can also be reduced by introducing Michaelis-Menten degradation rates that lower Hill coefficients at the expense of adding more parameters to the model. We retain the Relogio et al. [17] approach due to the nice model calibration with data. The rest of the protein concentrations in cytoplasmic forms given by $CRY_c(z_1)$, $PER_c(z_2)$, PER_c^*(phosphorylated form, z_3), $PER_c^*/$ $CRY_c(z_4)$, $PER_c/CRY_c(z_5)$ and nuclear form given by $PER_N^*/CRY_N(x_2)$, $PER_N/CRY_N(x_3)$, $PER/CRY_{pool}(x_2 + x_3)$ are given by simple law of mass action terms

$$\frac{dz_1}{dt} = k_{p2}(y_2 + y_{20}) + kd_{z4}z_4 + kd_{z5}z_5$$
$$- kf_{z5}z_1z_2 - kf_{z4}z_1z_3 - d_{z1}z_1 \quad (3)$$

$$\frac{dz_2}{dt} = k_{p1}(y_1 + y_{10}) + kd_{z5}z_5 + kd_{phz3}z_3$$
$$- kf_{z5}z_1z_2 - k_{phz2}z_2 - d_{z2}z_2 \quad (4)$$

$$\frac{dz_3}{dt} = k_{phz2}z_2 + kd_{z4}z_4 - kd_{phz3}z_3 - kf_{z4}z_3z_1$$
$$- d_{z3}z_3 \quad (5)$$

$$\frac{dz_4}{dt} = kf_{z4}z_1z_3 + ke_{x2}x_2 - ki_{z4}z_4 - kd_{z4}z_4 - d_{z4}z_4 \quad (6)$$

$$\frac{dz_5}{dt} = kf_{z5}z_1z_2 + ke_{x3}x_3 - ki_{z5}z_5 - kd_{z5}z_5 - d_{z5}z_5 \quad (7)$$

$$\frac{dx_2}{dt} = ki_{z4}z_4 - ke_{x2}x_2 - d_{x2}x_2 \quad (8)$$

$$\frac{dx_3}{dt} = ki_{z5}z_5 - ke_{x3}x_3 - d_{x3}x_3. \quad (9)$$

RBR Loop   This loop contains the clock genes Ror, RevErb, and Bmal and their corresponding proteins. In contrast to the inhibitory effect of PC proteins, the nuclear species ROR and REV/ERB participate in the regulation of Bmal in both inhibitory and activatory reactions, as shown in Fig. 1. Similar to the PC loop, mRNA production involves multiple nonlinearities and Michaelis-Menten terms

Rev-Erb $\dfrac{dy_3}{dt}$

$$= v_{3max} \frac{1 + g\left(\frac{x_1}{k_{t3}}\right)^6}{1 + \left(\frac{PC}{k_{i3}}\right)^2 \left(\frac{x_1}{k_{t3}}\right)^6 + \left(\frac{x_1}{k_{t3}}\right)^6} - d_{y3}y_3 \quad (10)$$

Ror $\dfrac{dy_4}{dt}$

$$= v_{4max} \frac{1 + h\left(\frac{x_1}{k_{t4}}\right)^6}{1 + \left(\frac{PC}{k_{i4}}\right)^3 \left(\frac{x_1}{k_{t4}}\right)^6 + \left(\frac{x_1}{k_{t4}}\right)^6} - d_{y4}y_4 \quad (11)$$

Bmal $\dfrac{dy_5}{dt}$

$$= v_{5max} \frac{1 + I\left(\frac{x_6}{k_{t5}}\right)^2}{1 + \left(\frac{x5}{k_{i5}}\right)^5 + \left(\frac{x_6}{k_{t5}}\right)^2} - d_{y5}y_5. \quad (12)$$

Similarly, the cytoplasmic protein forms REV-ERB$_c(z_6)$, ROR$_c(z_7)$, BMAL$_c(z_8)$ and nuclear forms REV-ERB$_N(x_5)$, ROR$_N(x_6)$, BMAL$_N(x_7)$, CLOCK/BMAL$_N(x_1)$ are given by simple law of mass action terms

$$\frac{dz_6}{dt} = k_{p3}(y_3 + y_{30}) - ki_{z6}z_6 - d_{z6}z_6 \quad (13)$$

$$\frac{dz_7}{dt} = k_{p4}(y_4 + y_{40}) - ki_{z7}z_7 - d_{z7}z_7 \quad (14)$$

$$\frac{dz_8}{dt} = k_{p5}(y_5 + y_{50}) - ki_{z8}z_8 - d_{z8}z_8 \quad (15)$$

$$\frac{dx_5}{dt} = ki_{z6}z_6 - d_{x5}x_5 \quad (16)$$

$$\frac{dx_6}{dt} = ki_{z7}z_7 - d_{x6}x_6 q \tag{17}$$

$$\frac{dx_7}{dt} = ki_{z8}z_8 + kd_{x1}x_1 - kf_{x1}x_7 - d_{x7}x_7 \tag{18}$$

$$\frac{dx_1}{dt} = kf_{x1}x_7 - kd_{x1}x_1 - d_{x1}x_1. \tag{19}$$

The system has 71 parameters of which 60 are derived from biological data and listed in [17]. The remaining 11 free parameters were fitted in [17] to fine tune the phase and amplitude relations between components of the model. We list the values of the parameters that we varied here from the reported values of Relogio et al. [17] in the Appendix; unless otherwise stated we use the parameter values of Relogio et al. [17] and refer to them as "wild type" in this study. The ODE model with these parameters generated oscillations with a period of 23.5 hours while also capturing the RNA and protein peak expressions in agreement with the ranges reported in the literature.

2.2 Stochastic Model

We created a stochastic analogue to these ODEs using methods previously described by [18]. Briefly, we seek to study the system response as the total number of molecules involved in the chemical reactions is reduced. This approach introduces intrinsic noise into the system that produces a rise in the amplitude of fluctuations around the system response predicted by the deterministic model of [17]; for a system containing N molecules the intrinsic noise amplitude is proportional to $1/\sqrt{N}$. For the stochastic model, we wrote a birth-death stochastic process with a corresponding master equation and transition probabilities between different system states. In our setting birth corresponded to a reaction step in which molecules were produced and death corresponded to molecules being consumed. The transition probabilities are thus proportional to the numbers of molecules and the chemical rate constant of each reaction described in the deterministic model. Since the ODE model is highly nonlinear, we followed the approach of [18] and decomposed the ODE reactions into 46 component elementary reactions. We then assigned a probability of occurrence to each elementary reaction using the reaction rates terms and parameter values from [17]. When computing reaction probabilities it is necessary to convert the units from concentrations to numbers of molecules, so we added a parameter Ω with units of volume. Ω represents the volume in which the reactions are occurring and can be thought of as the system size, where larger Ω implies a greater number of molecules involved. In broad strokes, the larger value of Ω the more the behavior of the stochastic system is expected to resemble that of the original ODEs.

As an illustration of our modeling approach we examine one elementary reaction and give its propensity that is then used in the stochastic simulations of the model. Specifically, an elementary reaction is the creation of the component z_5 from z_1 and z_2, or $z_1 + z_2 \rightarrow z_5$. The rate that drives this reaction forward from the ODE equation (7) is $kf_{z5}z_1z_2$. To compute a reaction propensity (or probability) we convert the rate by multiplying with the volume parameter Ω so that the propensity used in a stochastic simulation algorithm is $\frac{kf_{z5}}{\Omega}z_1z_2$. The rest of the reaction propensities were computed in a similar fashion and representative reactions are illustrated in the Appendix. The resulting system was then simulated using the Gillespie simulation technique [22], which associates a probability with each reaction and draws from an exponential distribution to compute a random reaction time. This simulation algorithm generates exact solutions for the stochastic birth death process underlying our stochastic model [22].

3 Results

As a first check for the correspondence between the deterministic and stochastic model we examined the qualitative behavior of our stochastic model as Ω was increased. Our simulation results shown in Fig. 2 indicate that at least qualitatively the stochastic model resembles closely the deterministic ODE model.

In cases where the internal noise is significant, i.e. Ω is small, the oscillations of the stochastic model are difficult to characterize in a non-qualitative fashion. The characteristic period of an oscillatory system under stochastic effects can be evaluated using autocorrelation analysis, which provides a comparison tool between the deterministic and stochastic oscillatory regimes. We define the autocorrelation function $F(\tau)$ for a biochemical species i with protein numbers given by N_i using

$$F(\tau) = \langle N_i(t+\tau)N_i(t) \rangle - \langle N_i(t) \rangle^2 \tag{20}$$

where $\langle \cdot \rangle$ denotes averaging with respect to time t. For systems that do not oscillate $F(\tau)$ decays monotonically, whereas for oscillatory systems the autocorrelation function shows damped oscillations. The average period of system oscillations (T) is marked by the location of the first peak of $F(\tau)$, whereas phase coherence is given by the total number of peaks in autocorrelation before it decays. To illustrate these ideas in Fig. 3(a) we plot the stochastic model average period for each model component against system size, Ω. For small system size, noise is significant and it causes sporadic model species oscillations as illustrated from the wide spread in periods for small Ω. Notably, different model components show different periods for small Ω. On the other hand, as the system size
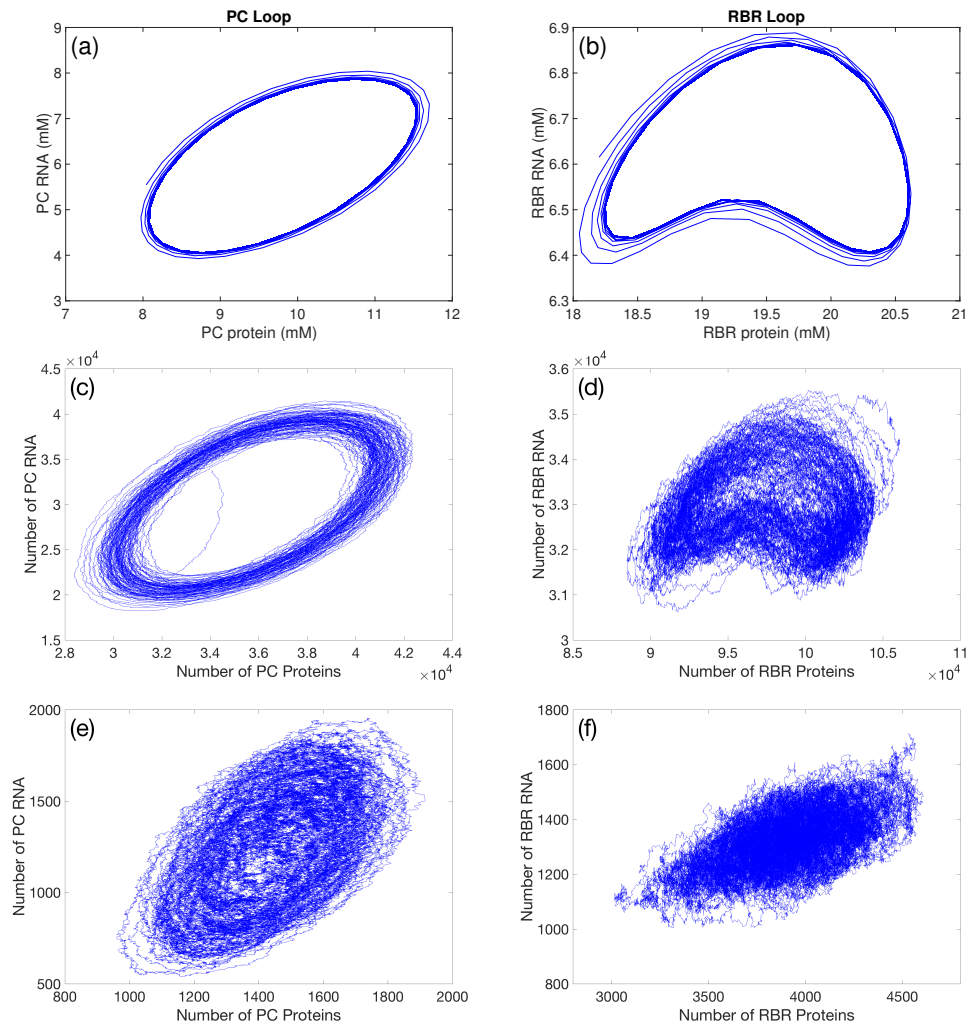
Figure 2: The behavior of the stochastic system as Ω is reduced. Top row (a), (b) shows the deterministic model; middle row (c), (d) shows $\Omega = 5000$; and bottom row (e), (f) shows $\Omega = 200$. The PC cycle shows RNA amounts of Per and Cry versus the total amount of PER and CRY protein. The RBR cycle shows RNA amounts of Ror, Bmal, and RevErb versus the total amount of ROR, BMAL, and REVERB protein. Note that the scale is changing as we reduce Ω.
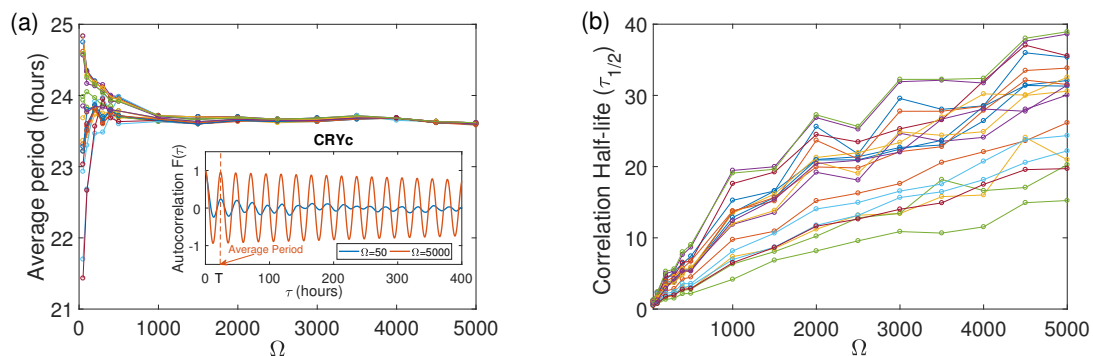

Figure 3: Autocorrelation function and correlation half-life. (a) Plot of the average stochastic model period as a function of Ω for all the model species. Inset. A representative autocorrelation function for CRYc species for $\Omega = 50$ and $\Omega = 5000$. (b) Plot of the correlation half-life $\tau_{1/2}$ for each model species as a function of Ω. Correlation half-life increases linearly with Ω indicating that periodic solutions strengthen as system size increases. All parameter values used correspond to the "wild type" values fitted in [17].

increases the average period for all components converges toward the deterministic model period of ≈ 23.5 hours. Besides the location of the peaks, autocorrelation can give an indication of the strength of the periodic signal since the $F(\tau)$ decay with different rates, where no decay indicates a perfect periodic signal and fast decaying peaks mark weaker periodic signals. In Fig. 3(a)(*inset*), we indeed see that $F(\tau)$ decays much faster when $\Omega = 50$ as opposed to $\Omega = 5000$ for the component CRY_c indicating that the periodic signal gains significant strength as Ω increases.

Fig. 3(a) illustrates that each model component can respond differently to noise for small Ω. Thus, next we separately examine each component by computing $F(\tau)$ on model time-courses, which are in turn obtained by Gillespie simulations of the stochastic system. We highlight that at the core of autocorrelation analysis is the assumption that each model component's individual time-course is well described by a single periodic signal disguised by noise. Thus, we represent $F(\tau)$ as a decaying oscillator and extract two pieces of information: 1) the period of the underlying signal, and 2) the rate at which that signal decays. The period is obtained by finding the location of the first peak of the autocorrelation $F(\tau)$ for each model species, as illustrated in Fig. 3(a). On the other hand, we measure the rate of decay of the damped oscillator using the half-life of the oscillations of the autocorrelation function (as defined in [18])

$$\hat{\tau}_{1/2} = \tau_A \ln 2 \qquad (21)$$

where τ_A is the standard correlation time measured as the rate of the decay of the autocorrelation function. We estimate τ_A numerically by measuring the autocorrelation decay rate using the exponential function $\exp(-t/\tau_A)$ that best fits the decay of the autocorrelation peaks. We remark that we expect the autocorrelation time to have a linear relationship with the size of the system Ω, as in [19, 18] it is shown that for their minimal circadian clock stochastic model the following relations hold

$$\hat{\tau}_{1/2} = \tau_A \ln 2 \approx \frac{\Omega \ln 2}{a} = \frac{\Omega w \ln 2}{\Omega_c} \qquad (22)$$

where Ω_c is the critical system size for the oscillations to remain correlated in time over more than one period and $w = 2\pi/T$. We remark that while appealing in its simple form, Ω_c shown in equation (22) is difficult to obtain analytically for our model given the high degree of nonlinearity. However, Ω_c can be related to the total number of molecules in the system. The total number of species X_i is $X_i = \Omega x_i$ and the maximum total number of molecules during one period of the oscillations is

$$N_{max} = \Omega \left(\sum_{i=1}^{s} x_i \right)_{max} \qquad (23)$$

with s marking the total number of components in the model. Thus for the system oscillations to remain correlated the total number of molecules which are present should be larger than the critical value

$$N = \sum_{i=1}^{s} X^i > \Omega_c \left(\sum_{i=1}^{s} x^i \right)_{max}. \qquad (24)$$

As shown in [18], Ω_c depends on the characteristic quantities of the system limit cycle, which in turn are tied to the form of the reactions prescribed for the ODE model and consequently reaction propensities in our stochastic version. Taken together these expressions indicate that the correlation time or the half-life provide a measure of the noise perturbations on the system since they directly depend on system size (or total protein numbers). We do not dwell on Ω_c details here, but note that in subsequent sections we choose a system size $\Omega = 2000 > \Omega_c$ for which all the species oscillations have $T_i \approx T_d$ corresponding to a tight distribution of periods around the deterministic period, $T_d \approx 23.5$.

In Fig. 3(b), we show measurements of the normalized correlation half-life defined here as $\tau_{1/2} = \hat{\tau}_{1/2}/T$ for each model component and observe a linear relation with Ω, as predicted by [19, 18]. Furthermore, we note that each model component displays its own scaling in correlation half-life ($\tau_{1/2}$) against Ω, which is to be expected since the linear relation in equation (22) depends on the maximal *total* number of molecules encoded in Ω_c, however each species' individual numbers can be either above or below this critical number, resulting in different slopes in Fig. 3(b). This means that each species has its own critical system size, even through the system as a whole can show oscillations similar to the deterministic limit. This is a major point of our study, and in the following sections we show how individual model component sensitivity can contribute or undermine overall system behavior in the stochastic model. To quantify these individual model component responses for the following section we fix $\Omega = 2000$ and compute a normalized autocorrelation half-life $\tau_{1/2}$ over a range of various parameter values. To most closely capture experimental procedures, we computed 10 realizations of the stochastic model per parameter value in Sections 3.1 and 3.2 and averaged the autocorrelation half-life over all trials. Each realization of the model was simulated for 800 hours, in order to allow ample sampling for the autocorrelation function analysis.

3.1 Autocorrelation analysis indicates differences in model architecture under internal noise.

In [17], two distinct oscillatory loops were postulated and tracked in the ODE deterministic system. Using our

stochastic model, we aim to see whether this two loop architecture is sustained under noise with the help of the correlation half-life, as defined above. We compute $\tau_{1/2}$ at $\Omega = 2000$ for the model components individually as a function of the Per mRNA degradation rate ($dy1$), a key parameter in determining the period of oscillations [5]. At the level of resolution of a single component of the model, there is too much information to detect any clear patterns from autocorrelation (Fig. 4(a)). We thus sum the components before calculating the correlation time by grouping all alternative forms of proteins, i.e. cytosolic, nuclear, phosphorylated, and unphosphorylated as shown in Fig. 4(b)–(c). We note this choice of clusters is biologically motivated and not based on the results of the model.

From the clustered model results for $\tau_{1/2}$, we see a clear pattern in the way that the components behave as a function of the mRNA degradation rate. Specifically, Per, Cry, and Ror along with their corresponding proteins form a single cluster, while RevErb, Bmal, and their corresponding proteins form another (Fig. 4(b)). This system structure that emerges from the autocorrelation corresponds to the two feedback loops proposed in Relogio et al. [17], with the exception that Ror and ROR cluster with the PC loop in our analysis. This indicates that the stochastic model presents a slightly different loop design than that proposed in the oscillator paradigm of the ODE model. This discrepancy is unexpected as we are studying the system in intermediate Ω-values, where a near deterministic system response seems to prevail. We can further capture the behavior of these putative clusters by summing all components in the Per, Cry, and Ror loop (PCRor) and separately summing the components of the RevErb and Bmal loop (RevBmal) (Fig. 4(d)). From Fig. 4(d), we see that the decay of autocorrelation oscillations of $F(\tau)$ as a function of the mRNA degradation rate differs qualitatively between the clustered PCRor and RevBmal loops. This analysis highlights that different portions of the circadian oscillator have different amounts of built-in robustness to noise, as measured by the decay of the autocorrelation function. Thus the structure of the mammalian oscillator might be susceptible to the effects of noise.

We further examined how the correlation half-life ($\tau_{1/2}$) of the summed clusters in the stochastic model changed with other model parameters studied in [17] (data not shown), and overall we observed a qualitatively different behavior of stochastic model loops from the original deterministic model. Specifically, from Fig. 4(d) it appears that a RevBmal loop maintains high $\tau_{1/2}$ for a wide range of $dy1$-values that we interpret as an indicator of strong periodic signal, as large correlation half-life corresponds to slow decay in $F(\tau)$, which in turn marks sustained oscillatory solutions. This use of $\tau_{1/2}$ as a marker of oscillatory response is also supported in Fig. 3(b) where we note

an overall increase in half-lifes of all model components for large Ω, where we know that the stochastic system oscillates in agreement with the deterministic model. On the other hand, in the same range of $dy1$ it seems that the $\tau_{1/2}$ in Fig. 4(d) points to a collapse in PCRor loop oscillations as marked by a steep decline in $\tau_{1/2}$-values for $dy1 > 1$. In the next section, we explore in more detail the correspondence between $\tau_{1/2}$ and transitions in and out of periodic solution regimes for the stochastic model. For now, we remark that by direct inspection of $\tau_{1/2}$ we see that the autocorrelation function could be used to detect varying sensitivity to intrinsic noise levels for each loop with one loop showing weaker periodic signal as model parameters are varied.

In conclusion, given the uncertainty and malleability of parameters in a biological system, the stochastic model indicates that two key loops emerge and respond independently to stochastic effects. The differences between the two loops was also observed in the deterministic system of [17] where they showed sustained periodic behavior of the RevBmal loop by artificially clamping a single component of the PC loop to a constant value. Yet, the stochastic model autocorrelation analysis presented here reveals the distinct model component oscillatory behavior without the need to force various components to constant values. In fact, in the concerned parameter region of $dy1$, we observe that the components of the PCRor loop continue to fluctuate in an aperiodic manner without interfering with the oscillatory behavior of the other loop, Fig. 4(d) (note the small bump in PCRor $\tau_{1/2}$ for $1 < dy1 < 4$ which indicates a slightly higher half-life in PCRor fluctuations while RevBmal maintains high $\tau_{1/2}$). We note the connection between our qualitative observations of $\tau_{1/2}$-values and bifurcation analysis in the deterministic system; both are concerned with identifying the parameter regions where the respective model is likely to oscillate. However, a more systematic comparison is necessary and we pursue this next.

3.2   Bifurcations in the Stochastic System.

In order to probe the response of the stochastic model in varying parameter regimes, we computed numerically using XPPAUTO [23] the bifurcation diagrams of the ODE model in [17] (shown in Fig. 5-insets) and compared them with our autocorrelation analysis results. When comparing the deterministic bifurcation diagrams to our stochastic model in near-deterministic, i.e. ($\Omega = 2000$), conditions we see a clear pattern where by the RevBmal loop has a stronger underlying periodic signal in parameter regions which are periodic in the deterministic system. This suggests that the Hopf bifurcations in the deterministic system are closely mirrored in the stochastic model.
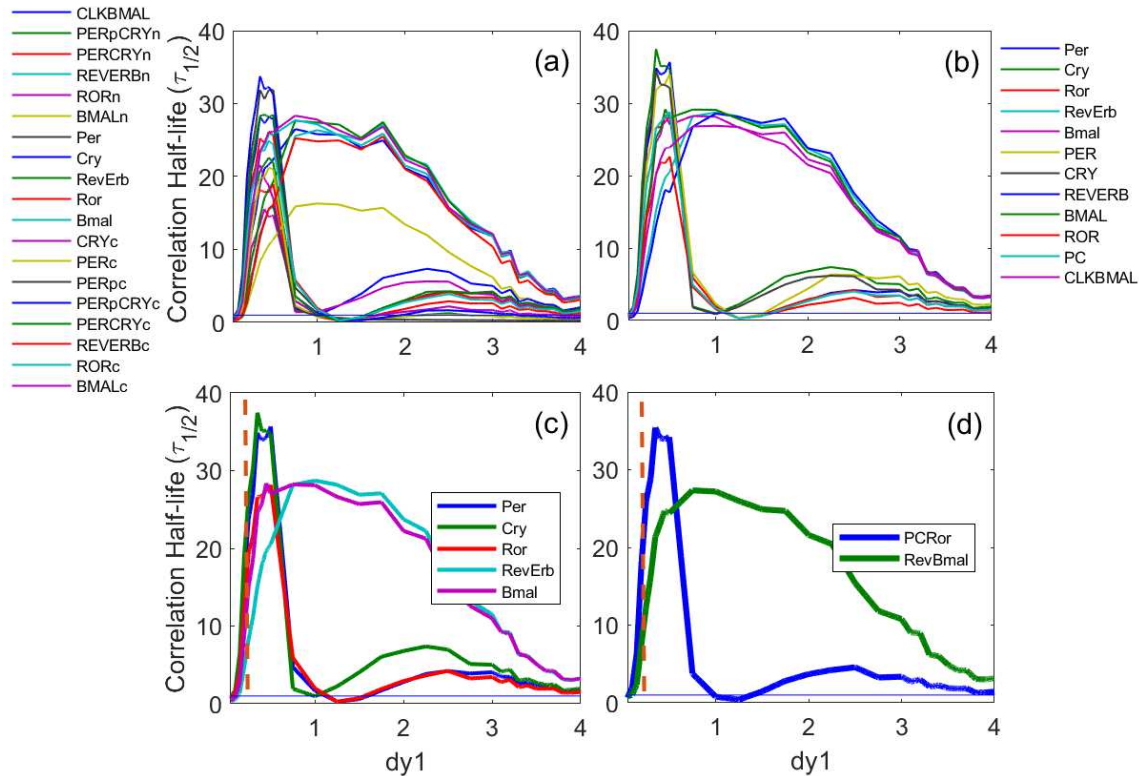
Figure 4: Autocorrelation analysis of components with $\Omega = 2000$. On the y-axis is the correlation half-life ($\tau_{1/2}$), an inverse measure of the amount of noise in the signal. On the x-axis is the parameter $dy1$, which describes the rate of decay of the Per mRNA. The relation between these are shown for (a) each of the 19 components individually, (b) with alternate forms of the same protein, i.e. cytosolic and nuclear forms of PER, summed together before analysis, (c) with only the mRNA components represented, and (d) all components of each cluster are summed. PCRor contains Per, Cry, Ror, and their corresponding protein forms. RevBmal contains Bmal, Rev, and their corresponding protein forms. Results shown are averages over 10 identical trials. Wild-type parameter value for $dy1 = 0.3$ (hour)$^{-1}$ from [17] is shown as a vertical dotted line in (c) and (d).

To quantify similarities and discrepancies in the bifurcation structure between the deterministic and stochastic system, we quantified the location of bifurcation-like points in the stochastic model using an "optimized-thresholding" algorithm.

- First, we examined the behavior of the correlation half-life $\tau_{1/2}$ around the Hopf bifurcation points in the deterministic bifurcation diagrams (Fig. 5). For the sum of all components in the system when $\Omega = 2000$ (data not shown), a simple threshold of $\tau_{1/2} = 1$ produces stochastic bifurcation values close to the deterministic bifurcation values. This suggests a useful equivalence between a $\tau_{1/2}$ near zero and a bifurcation in the deterministic system, and we sought to extend this to lower values of Ω.

- As the values of $\tau_{1/2}$ are very sensitive to Ω (Fig 3) and vary for each loop, instead of using a set arbitrary system threshold of $\tau_{1/2} = 1$, we chose to work with a set relative drop in $\tau_{1/2}$ signal from the maximum $\tau_{1/2}$. Specifically, for each Hopf bifurcation

point, we calculated the % drop between the maximum $\tau_{1/2}$ value and the $\tau_{1/2}$ value where system $\tau_{1/2} = 1$ for both the RevBmal and the PCRor loop when $\Omega = 2000$. This provides distinct thresholds and corresponding estimated bifurcation-like points for each loop.

- In order to ensure the useful connection between the stochastic bifurcation-like points and the deterministic Hopf bifurcation points, out of the two loops, we chose to work with the % drop of the loop whose estimated bifurcation-like point was closest to the deterministic bifurcation point. We then adjusted this % drop such that the estimated bifurcation point corresponded more closely to the deterministic Hopf point for large Ω. We next used this "optimized" % drop threshold for both loops and all Ω-values. Note that for small Ω, this approach can become unstable as noise begins to dominate the measurements of $\tau_{1/2}$.

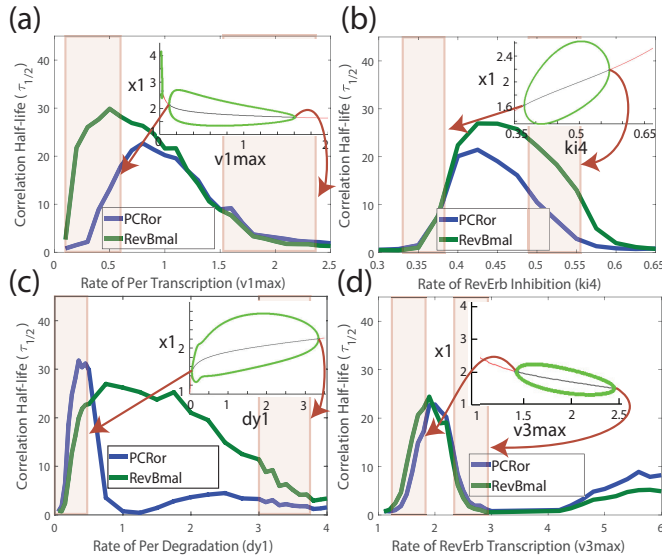This adaptive strategy ensures that the bifurcation-like points converge to the deterministic Hopf point for large

Figure 5: Deterministic bifurcation plots vs stochastic autocorrelation half-life. The autorrelation half-life ($\tau_{1/2}$) is computed for each parameter value shown on the x-axis and binned into two highlighted regions around the deterministic Hopf points. The corresponding deterministic bifurcation diagrams in the same parameter range are shown in each figure inset.
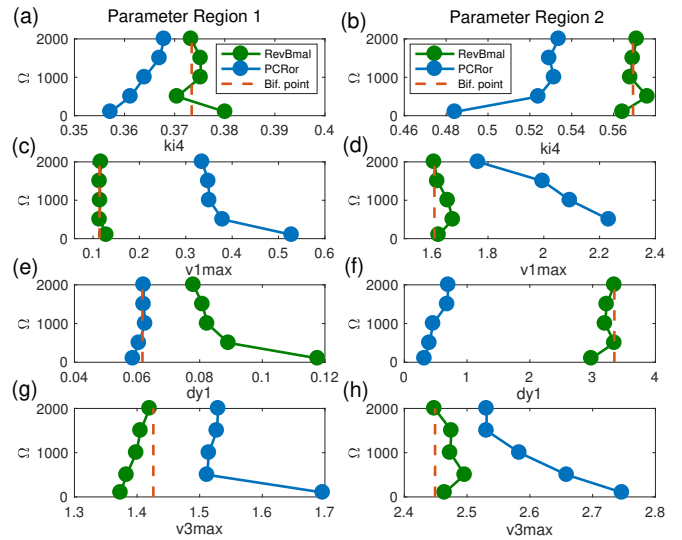

Figure 6: Bifurcations of PCRor and RevBmal loops are distinct. Vertical dotted lines represent the locations of the deterministic Hopf bifurcation points. Left and right panels show results for two relevant parameter regions around the Hopf points in the deterministic model. The lines represent how the bifurcation analogues in the stochastic system change with system size for the RevBmal and PCRor loop in the a) Ror inhibition rate (k_{i4}), b) Maximum Per transcription rate (v_{1max}), c) Per mRNA degradation rate (d_{y1}), and d) Maximum RevErb transcription rate (v_{3max}).

Ω and also allows for different loops to control each bifurcation. For example, if we examine the first bifurcation point for $dy1$ in Fig. 5(c), we note that the values of τ for the PCRor loop are higher than the RevBmal. Appropriately, in Fig. 6(e), we see that the bifurcation-like point of the PCRor loop converges to the deterministic Hopf point. These bifurcation-like points or "stochastic bifurcations" allow us to examine the relative sensitivities of each loop separately against changes in parameter values as well as system size Ω.

With this method, we noted two key system features: 1) the bifurcations of the PCRor loop often appeared independent of that of the RevBmal loop, and, 2) that the locations of the bifurcations points change with Ω. Specifically, we noted that in some cases, the oscillatory parameter regions shrunk or expanded with the system size, in other cases the opposite was true. There were even instances where the acceptable parameter region appeared to shift between the two loops, as highlighted by the relative position of the stochastic bifurcation points with the deterministic values shown as dotted lines in Fig. 6. These observed trends in stochastic bifurcation points are related to the shape of the correlation half-life functions for each parameter, as shown in Fig. 5; notably for $dy1$ we saw that the PCRor loop increased faster than the RevBmal loop in parameter region 1, however, it also dropped much faster than the RevBmal loop-these caused the reversal in bifurcation point ordering reported in Fig. 6.

In the analysis of the deterministic ODEs, the location of the Hopf bifurcation were controlled by the driver loop, RevBmal. When this loop was oscillating or "turning" it was able to keep the other, PCRor, loop turning as well. In a sense this means that the "strength" of the RevBmal loop allows the system to tolerate the failure of the other component. Yet in the corresponding stochastic system, this is not the case. The PCRor loop is more, and in some case much more, sensitive to the parameter values chosen: both in that the parameter regions where periodic-like behavior is maintained is smaller than that of RevBmal (Fig. 5) and in that as the system size (Ω) changes the bifurcation-like points shift more dramatically (Fig. 6). In the biological system, the failure of the PCRor loop would be felt as an aperiodic regulation of gene expression via the PC complex. We note that our stochastic model allows us to reach an important conclusion. Namely, by restricting the analysis to the deterministic realm, one reaches erroneous conclusions about the prediction of the model about the driver loop for the system. Whether or not this is an artifact of the particular network topology is something that remains to be explored. This conclusion also calls into question the concept that more feedback loops increase the robustness of oscillating behavior in biological systems.

4 Wavelet Analysis Reveals Transient Lapses in Periodicity.

Autocorrelation analysis, while useful in the context of noisy data and stochastic models, has shortcomings due to fundamental assumption that the intrinsic period and amplitude of the time series under consideration do not change over time. When a periodic signal presents significant variation in amplitude and period, as our model and typical circadian data do, then autocorrelation cannot tell us how the period may vary as a function of time. Thus important information can be lost if one focuses just on autocorrelation. Wavelet based approaches can prove more effective for determining period length along with a measurement of the variability in period and amplitude in time, reviewed in [24]. Wavelet analysis aims to decompose a signal as a sum of component waveforms. In contrast to Fourier analysis, wavelets are localized (or windowed) in time in such a way that the temporal duration of the window is adjusted to each frequency being analyzed. We employ a continuous wavelet transform (CWT), which for a complex valued wavelet function $\Psi(t)$ can be defined as

$$W(t,s) = \int \frac{1}{s}\Psi^*\left(\frac{u-t}{s}\right)x(u)du \qquad (25)$$

with ψ^* is the complex conjugate. At a time t, the period of the signal is identified by changing the scale (s) that maximizes the wavelet transform between the signal and the scaled wavelet. To analyze the signal one generates the so called wavelet ridge curves, which run along the local maxima with respect to period, s of the absolute value of the CWT. The absolute value of the CWT in turn marks the signals instantaneous frequency and amplitude at each time point.

Following [20], we use Morlet wavelets to analyze the stochastic model. The Morlet wavelet function is given by

$$\Psi(t) = \exp(iw_0 t)\exp\left(-\frac{t^2}{2\sigma^2}\right), \qquad (26)$$

where w_0 is the frequency and σ is a measure of the spread of the support. By applying a Morlet wavelet centered at t to our model results, we can calculate periodic decomposition of the model time course at time t with the advantage that wavelet analysis does not assume a single dominant periodic signal, an assumption that causes the autocorrelation to become biased when, for example, there is a skipped period [20]. Following, [20] the Morlet wavelet applied to a data series generates a table of complex values for varying s and t, with heat map plots arising from consideration of the magnitude of the complex values, illustrated in Fig. 7.

The local maxima of the magnitude of the wavelet transform at each time point correspond to the ridges illustrated both in the heat maps (blue line overlay) and ridge strength plots in Fig. 7. Each ridge point location on the period axis of the CWT magnitude heat map indicates the *dominant oscillatory period* for the system at the indicated time. We employ the algorithm of [20, 25] to compute and plot the CWT ridges to monitor the dominant period of the cell over time.

Examining the wild type behavior of the system using the CWT magnitude and CWT ridges reveals a surprising behavior that is hidden from autocorrelation analysis. For short time spans, the strength of the periodic signal as measured by the ridge strength drops dramatically, illustrated in Fig. 8 where we show three realizations of the model with the same parameter values. As the Morlet analysis is windowed, this transition is smooth, but this implies that the periodic behavior is punctuated by aperiodic behavior for the stochastic model. Unlike the above autocorrelation analysis, where one loop continues while the other halts, both loops appear here to lapse simultaneously as illustrated in Fig. 9.

The frequency and length of these aperiodic anomalies appears to be modified with system size in the stochastic model. To illustrate how the time spent in aperiodic behavior changes with the system size Ω, we present histograms of the ridge strength of RevBmal and PCRor loops normalized to the mean ridge strength for each Ω (Fig. 10). From the density plots in Fig. 10, we observe that the variation around the mean in ridge strength increases as Ω is decreasing, indicating that for small Ω the system spends a large fraction of time with very weak periodic signal. These observations could provide an alternate explanation for some experimental results [9, 8]. In these studies, the authors observed circadian oscillation of mouse SCN cells at single cell resolution either in tissue slices or in isolated cells. Reanalysis of this data by Meeker et al. [20] found that while cells in slices maintained strong periodic behavior, isolated cells displayed the occasional highly elongated period. Our alternate explanation is that this elongated period could actually represents transient aperiodic behavior among isolated cells. While Meeker et al. [20] was able to fit their model to explain the data, we obtain similar behavior at the wild type parameter values fitted by Relogio et al. [17] that are supposed to support normal periodic behavior in the deterministic model. This finding provides additional evidence that the stochastic model displays qualitatively different behavior than the deterministic model despite identical parameter values, indicating that low protein numbers can significantly alter system behavior for the mammalian circadian oscillator.
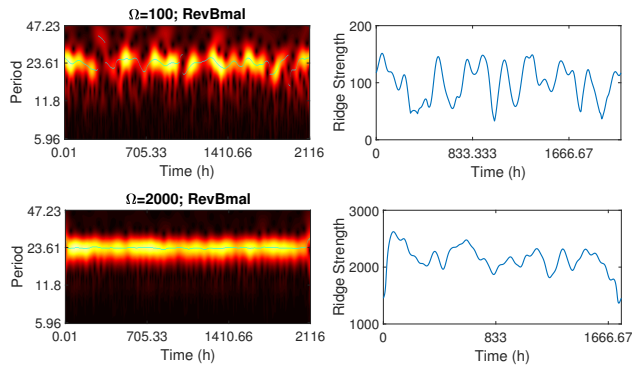
Figure 7: Morlet wavelet analysis of the RevBmal loop for two Ω-values. CWT magnitude heat map and ridge strengths are shown for (a) $\Omega = 100$, (b) $\Omega = 2000$.
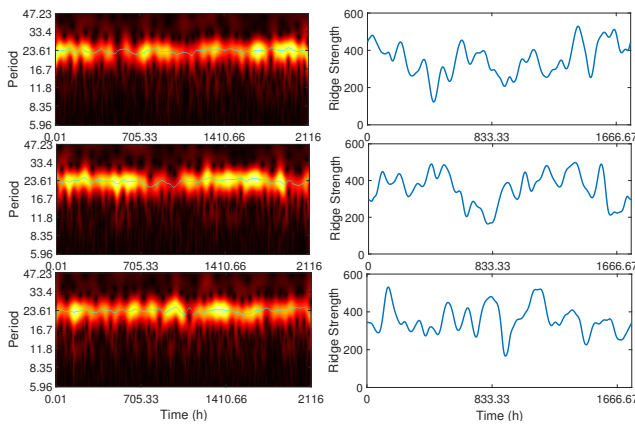

Figure 8: Transient lapses in stochastic model periodicity for $\Omega = 400$. Triplicate heat maps visualizing the Morlet wavelet analysis are calculated from the same parameters as in [17] for three distinct realization of the model shown in each row. The height of the ridges for each corresponding calculation is shown on the right column panels.
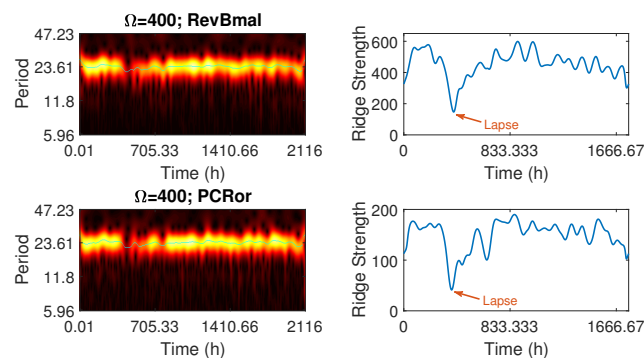

Figure 9: Transient lapses in both loops of the stochastic model periodicity for $\Omega = 400$. Heat maps visualize the Morlet wavelet analysis with parameters same as in [17]. The height of the ridges for each corresponding calculation is shown on the left panels.
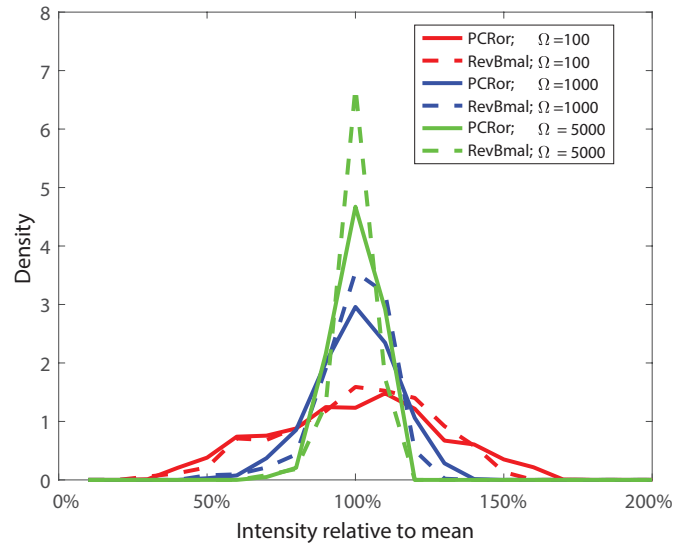

Figure 10: Histogram of the intensity of periodic signal for different system sizes relative to the mean intensity for each system size. The mean intensity is calculated across the strongest periodic signal for each Ω. The intensities of the strongest periodic signal at each given time are then shown relative to this mean and assembled in a histogram. For example, the density at 40% represents the fraction of time spent where the intensity of the maximum periodic signal is only 40% as strong as the mean value.

5   Discussion

Circadian rhythms represent a fundamental way that organisms respond to daily changes in the environment and, in humans, an important health consideration [2, 3]. Modeling of these chemical clocks has often focused on deterministic systems of ODEs [6, 12, 13], but biological data suggest that noise can influence these rhythms [7, 10]. Given observations that molecules controlling these rhythms are present in very low numbers [15], stochastic models that explicitly track each protein number as they undergo reactions in time represent a computational modeling strategy that can reveal biologically relevant behavior that might not be observed in deterministic mathematical models that average system behavior in the limit of large protein numbers. For example, deterministic and stochastic mathematical models of circadian clocks have been observed in prior work to predict qualitatively different behavior for specific mutants [26] or display shifting periods over time [20].

In this paper, we developed a stochastic birth-death model that builds upon a previously proposed deterministic model for the mammalian circadian rhythm in [17]. We used the Gillespie [22] algorithm to simulate the stochastic model and then analyzed the results for varying system sizes and parameter values. We used a scaled

correlation time quantity in order to study the strength of periodic signal present in the stochastic model and further employed it in order to test the robustness to noise of various model sub-components that were postulated as important building blocks in the ODE model. We found that the stochastic model components could be classified into sub-clusters that differed slightly from the clusters proposed in the ODE model, notably with Ror clustering with the PC loop. We next used correlation half-life to build a stochastic version of the bifurcation diagram of the ODE model in order to test the robustness of the Hopf points in the stochastic model for different system sizes and with respect to different parameters. We found that the stochastic system showed varying levels of sensitivity to noise as the predicted correlation half-life Hopf points varied when Ω was changed. Further, we noted that the two loops of the stochastic model had different Hopf points, and thus confirmed the independence in their oscillatory behaviors. Biologically, this last finding indicates that additional negative feedback loops do not necessarily confer greater robustness to an oscillatory system under noise perturbation. The opposite may be true, in that that the flexibility and independence of a second loop allows rapid phase changes to be made. For example, the model used here could transiently lapse into aperiodic behavior.

Since autocorrelation analysis loses time information, we next performed wavelet analysis in order to test the stochastic model variations in periods as a function of time. We found that the stochastic model can show transient lapses in periodicity particularly in low system size regimes. This behavior is of interest as the model was being examined in "wild type" parameter ranges where the deterministic model showed robust oscillations. The primary goal of this work was to explore the role of intrinsic noise that arises in the case of low protein numbers on a detailed and robust mammalian circadian clock ODE model. We found that the stochastic model can show both different behavior in terms of oscillatory regimes and lapses in periodicity when compared with the ODE model in the same parameter ranges. Most importantly, the stochastic model when probed through autocorrelation analysis showed that under noise perturbation model components could cluster differently between the two key circadian clock feedback loops, indicating that system architecture could be affected by internal noise.

The autocorrelation and wavelet analysis of our stochastic model is likely more amenable to quantifying experimental data from noisy oscillators in biochemical networks, particularly when trying to detect network topology. It is important to note that the contrast between the two loops architecture we noted here is likely detectable in the autocorrelation from the mRNA levels alone, suggesting that system architecture might be un-

covered more systematically by devising models that can capture noisy data and then examining the deterministic limits that produce ODE that are more amenable to analysis. In this context, we expect that a stochastic modeling approach is an important and necessary tool in examining circadian oscillator properties. Indeed, our stochastic model analysis does not ignore fluctuations in low protein number regimes but instead relies on them in order to test system response as various model parameters are varied. ODE models necessarily ignore these low protein level effects and impose a feedback structure that can only match the biological system response in the sense of averages, ignoring the important role of fluctuations.

Finally, we highlight that despite a significant amount of modeling in this field, the key network motifs comprising the circadian oscillator are still debated. Recently, using a carefully parametrized ODE model in [27], a large computational effort was put into systematically clamping all possible combinations of gene-subsets to their oscillation mean values in the model in order to uncover the necessary and sufficient sub-networks needed for self-sustained circadian oscillations. Our analysis shows that a stochastic model might vary in its response and loop architecture when compared with its deterministic equivalent ODE model, so one must be careful when drawing conclusions about system architecture that rely solely on ODE model analysis. We propose that stochastic versions of these models should also be examined and compared with noisy data when trying to assess overall network topology.

Appendix

Wild type parameters

The model has 71 parameters as described in [17], of which 11 were fitted. In Table 1 we list the parameter values used in [17] that are relevant to our study in Section 3.2. We refer to these values as "wild type" parameter values in the manuscript since they yield wild type circadian oscillations for the ODE model.

Reaction propensities

In Table 2 we show some illustrative elementary reactions for the stochastic model along with their reaction propensities (or probabilities) as used for the Gillespie simulations.

Parameter	Description	Value
dy1	Degradation rate for Per mRNA (hour^{-1})	0.3
ki4	Ror-inhibition rate (a.u)	0.4
v1max	Per transcription rate (a.u.-hour^{-1})	1
v3max	RevErb transcription rate (a.u.-hour^{-1})	1.9

Table 1: "Wild type" parameter values for the stochastic model.

Reaction	Description	Probability of Reaction
$G_i \overset{v_{imax} f(x_1, x_5, x_6)}{\rightarrow} M_{yi}$	Transcription of gene (G_i) into mRNA (M_{yi})	$w_a = v_{imax} f(x_1, x_5, x_6)\Omega$
$M_{yi} \overset{k_{pj}}{\rightarrow} P_{zj}$	Cytoplasmic protein(P_{zj}) production	$w_b = k_{pj} M_{yi}$
$P_{zj} + P_{zi} \overset{kf_{zc}}{\rightarrow} P_{zc}$	Cytoplasmic complex (P_{zc}) formation	$w_c = kf_{zc} P_{zi} P_{zj}/\Omega$
$P_{zj} \overset{ki_{zj}}{\rightarrow} P_{xi}$	Nuclear protein shuttling	$w_d = ki_{zj} P_{zj}\Omega$

Table 2: Representative reactions for the stochastic model. The function $f(x_1, x_5, x_6)$ represents a Michaelis-Menten rate term, as described in Section 2.1 with protein nuclear forms REV-ERB$_N(x_5)$, ROR$_N(x_6)$, CLOCK/BMAL$_N(x_1)$.

References

[1] Joseph S Takahashi. Transcriptional architecture of the mammalian circadian clock. *Nature Reviews Genetics*, 2016.

[2] Sahar Farajnia, Tom Deboer, Jos HT Rohling, Johanna H Meijer, and Stephan Michel. Aging of the suprachiasmatic clock. *The Neuroscientist*, 2013.

[3] Yuanwei Huang, Qiuyan Yu, Yan Liu, Zhenli Zhu, Li Wang, Haidong Wang, and Ke Li. Efficacy and safety of chronomodulated chemotherapy for patients with metastatic colorectal cancer: a systematic review and meta-analysis. *Asia-Pacific Journal of Clinical Oncology*, 2016.

[4] William Bechtel. From molecules to networks: Adoption of systems approaches in circadian rhythm research. In *New Challenges to Philosophy of Science*, pages 211–223. Springer, 2013.

[5] Carrie L Partch, Carla B Green, and Joseph S Takahashi. Molecular architecture of the mammalian circadian clock. *Trends in cell biology*, 2013.

[6] Albert Goldbeter. A model for circadian oscillations in the drosophila period protein (per). *Proceedings of the Royal Society of London. Series B: Biological Sciences*, 261(1362):319–324, 1995.

[7] Erik D Herzog, Sara J Aton, Rika Numano, Yoshiyuki Sakaki, and Hajime Tei. Temporal precision in the mammalian circadian system: a reliable clock from less reliable neurons. *Journal of biological rhythms*, 19(1):35–46, 2004.

[8] Alexis B Webb, Nikhil Angelo, James E Huettner, and Erik D Herzog. Intrinsic, nondeterministic circadian rhythm generation in identified mammalian neurons. *Proceedings of the National Academy of Sciences*, 106(38):16493–16498, 2009.

[9] Andrew C Liu, David K Welsh, Caroline H Ko, Hien G Tran, Eric E Zhang, Aaron A Priest, Ethan D Buhr, Oded Singer, Kirsten Meeker, Inder M Verma, et al. Intercellular coupling confers robustness against mutations in the scn circadian clock network. *Cell*, 129(3):605–616, 2007.

[10] Naama Barkai and Stanislas Leibler. Biological rhythms: Circadian clocks limited by noise. *Nature*, 403(6767):267–268, 2000.

[11] Olga A Podkolodnaya, Natalya N Tverdokhleb, and Nikolay L Podkolodnyy. Computational modeling of the cell-autonomous mammalian circadian oscillator. *BMC Systems Biology*, 11(1):27, 2017.

[12] Didier Gonze and Albert Goldbeter. Circadian rhythms and molecular noise. *Chaos: An Interdisciplinary Journal of Nonlinear Science*, 16(2):026110–026110, 2006.

[13] Jae Kyoung Kim and Daniel B Forger. A mechanism for robust circadian timekeeping via stoichiometric balance. *Molecular systems biology*, 8:630, 2012.

[14] Martha W Merrow, Norman Y Garceau, and Jay C Dunlap. Dissection of a circadian oscillation into discrete domains. *Proceedings of the National Academy of Sciences*, 94(8):3877–3882, 1997.

[15] Kiho Bae, Choogon Lee, Paul E Hardin, and Isaac Edery. dclock is present in limiting amounts and likely mediates daily interactions between the dclock–cyc transcription factor and the per–tim complex. *The Journal of Neuroscience*, 20(5):1746–1753, 2000.

[16] Darren J. Wilkinson. Stochastic modelling for quantitative description of heterogeneous biological systems. *Nat Rev Genet*, 10(2):122–133, February 2009.

[17] Angela Relógio, Pal O Westermark, Thomas Wallach, Katja Schellenberg, Achim Kramer, and Hanspeter Herzel. Tuning the mammalian circadian clock: robust synergy of two loops. *PLoS computational biology*, 7(12):e1002309, 2011.

[18] Didier Gonze, José Halloy, and Albert Goldbeter. Robustness of circadian rhythms with respect to molecular noise. *Proceedings of the National Academy of Sciences*, 99(2):673–678, 2002.

[19] Didier Gonze, José Halloy, and Pierre Gaspard. Biochemical clocks and molecular noise: Theoretical study of robustness factors. *The Journal of chemical physics*, 116:10997, 2002.

[20] Kirsten Meeker, Richard Harang, Alexis B Webb, David K Welsh, Francis J Doyle, Guillaume Bonnet, Erik D Herzog, and Linda R Petzold. Wavelet measurement suggests cause of period instability in mammalian circadian neurons. *Journal of biological rhythms*, 26(4):353–362, 2011.

[21] Anja Korenčič, Grigory Bordyugov, Damjana Rozman, Marko Goličnik, Hanspeter Herzel, et al. The interplay of cis-regulatory elements rules circadian rhythms in mouse liver. *PLoS One*, 7(11):e46835, 2012.

[22] Daniel T Gillespie. Exact stochastic simulation of coupled chemical reactions. *The journal of physical chemistry*, 81(25):2340–2361, 1977.

[23] B Ermentrout. Xppaut®–the differential equations tool, version 5.98; 2006.

[24] Tanya L Leise and Mary E Harrington. Wavelet-based time series analysis of circadian rhythms. *Journal of biological rhythms*, 26(5):454–463, 2011.

[25] Richard Harang, Guillaume Bonnet, and Linda R Petzold. Wavos: a matlab toolkit for wavelet analysis and visualization of oscillatory systems. *BMC research notes*, 5(1):163, 2012.

[26] Daniel B Forger and Charles S Peskin. Stochastic simulation of the mammalian circadian clock. *Proceedings of the National Academy of Sciences of the United States of America*, 102(2):321–324, 2005.

[27] J Patrick Pett, Anja Korenčič, Felix Wesener, Achim Kramer, and Hanspeter Herzel. Feedback loops of the mammalian circadian clock constitute repressilator. *PLOS Computational Biology*, 12(12):e1005266, 2016.